PAPER

Check for updates

Waste plastic derived nitrogen-doped reduced graphene oxide decorated core–shell nano-structured metal catalyst (WpNrGO-Pd–Ru) for a proton exchange membrane fuel cell

Sunil Dhali,[a] Manoj Karakoti,[ae] Gaurav Tatrari,[a] Sandeep Pandey,[a] Kundan Singh Rawat, ID [a] Chetna Tewari,[b] Boddepalli Santhi Bhushan,[c] Yong Chae Jung, ID [b] Anurag Srivastava ID [d] and Nanda Gopal Sahoo ID *[a]

Waste plastic-derived nitrogen-doped reduced graphene oxide (WpNrGO) was demonstrated for the first time as a catalyst support for PEMFCs. WpNrGO plays a significant role in enhancing the efficacy and durability of electrocatalysts for PEMFCs. Graphene nanosheets (GNs) are obtained by upcycling waste plastic *via* pyrolysis, followed by the modified Hummers' method to obtain WpGO. WpNrGO was produced by the thermal annealing of WpGO with urea (NH_2CONH_2) at 750 °C. Further, a WpNrGO-supported palladium–ruthenium (Pd_Ru) electrocatalyst was synthesized with Pd : Ru concentration in the ratio 2 : 1. Synopsys-QuantumATK was used to run DFT-based first principles simulations to comprehend the ideal locations for adsorption on GNs. The resulting WpNrGO-supported Pd_Ru (2 : 1) core–shell electrocatalyst demonstrated a higher electrochemical surface area (ECSA) of ~43 m^2 g^{-1} for the oxygen reduction reaction (ORR) and half potential of 0.33 V, along with high catalytic activity and stability.

1. Introduction

Over the past few years, significant environmental problems have arisen due to the burgeoning production as well as improper management and distribution of waste materials. These waste materials may include plastic waste, food waste, medical waste, *etc.* These have significant and widespread negative effects on the environment and health, undoubtedly contributing to the spread and emergence of various deadly diseases. Additionally, these are responsible for increasing global temperatures, causing the earth to erode and flood, and other environmental calamities.

[a] Prof. Rajendra Singh Nanoscience and Nanotechnology Centre, Department of Chemistry, Kumaun University, DSB Campus, Nainital-263001, India. E-mail: ngsahoo@yahoo.co.in

[b] Institute of Advanced Composite Materials, Korea Institute of Science and Technology (KIST), 92 Chudong-ro, Bongdong-eup, Wanju-gun, Jeonbuk, 55324, Republic of Korea

[c] Department of Electronics and Communication Engineering, Indian institute of Information Technology, Allahabad-211015, India

[d] Advanced Materials Research Group, CNT Lab, ABV - Indian Institute of Information Technology and Management, Gwalior, Madhya Pradesh, 474015, India

[e] Institute of Macromolecular Chemistry, Academy of Science of the Czech Republic, Prague 6, 16206, Czech Republic

Apart from solid waste, green and alternative energy sources are a prime requirement in the present context. Currently, fossil fuels are being used to meet the world energy needs. There are two main problems with the continuous use of these fuels: environmental challenges and longevity. According to the Petroleum Corporation, the production peak of petroleum and natural gas will be between 2020 and 2027 before beginning to decline.[1] Therefore, people are turning towards fuel cells because they exhibit high efficiency (as high as 60%) with almost zero carbon emissions, making them a considered green energy source. Currently, various types of fuel cells are known, and these are divided into alkaline fuel cells (AFCs),[2,3] proton exchange membrane fuel cells (PEMFCs),[4,5] phosphoric acid fuel cells (PAFCs),[6] molten carbonate fuel cells (MCFCS),[7] solid oxide fuel cells (SOFCs),[8] and so on.

PEMFCs are a very popular choice among various fuel cells owing to their numerous advantages, including the ability to operate at low temperatures, making them easier to contain and reducing thermal losses. Moreover, PEMFCs are extremely lightweight and smaller in volume, and therefore, these are suitable for automotive and portable applications. In PEMFCs, catalysts play a significant role in their performance. Currently, platinum (Pt) as a catalyst with a carbon (C) support has been frequently used.[9] However, the higher cost of Pt limits its extensive use in PEMFCs. In addition, the agglomeration of

Pt in Pt/C and the instability of Pt/C in acidic environments pose significant challenges. Therefore, the replacement of Pt with other metal catalysts and carbon with graphene and CNT derivatives can be a great choice for catalyst application.[10] In this context, many metals such as Pd, Fe, Ru, Co and their bimetallic combination as catalysts and CNMs (graphene, graphene oxide, and heteroatom-doped graphene) as a catalyst support have been used in PEMFCs. Nitrogen-doped catalyst supports are considered effective in enhancing the properties of carbon nanomaterials inherently, owing to their analogous atomic size and the ability to form active, strong bonds with carbon atoms. The doping of nitrogen in CNMs plays a crucial role in regulating electrons and enhancing the durability of carbon nanomaterials.[11] In addition, recent research has shown that NGO has better electrocatalytic activity for ORR, and methanol oxidation demonstrates good performance in energy storage devices than pure graphene.[12–17]

Although significant advancements have been made in graphene-based catalysts for the oxygen reduction reaction (ORR), particularly when they are loaded with metal nanoparticles. But, the nitrogen-doped core–shell structured bimetal catalysts have been explored far less. Within this context, Ramirez-Barria *et al.* explained that NGO enhanced the catalytic activity and showed that the conversion of benzyl alcohol increased five times in aerobic oxidation conditions.[18,19] Furthermore, it was reported by Zhang *et al.* and Liang *et al.* that nitrogen-doped graphene catalysts exhibited excellent catalytic performance in acidic media, with superior onset potential, electron transfer, durability, tolerance against methanol crossover, and carbon monoxide poisoning.[20,21] Similarly, Dong *et al.* found that graphene-supported Pt/Ru showed significantly enhanced performance for both methanol and ethanol electrooxidation.[22] Awasthi *et al.* showed that graphene-assisted Pd/Ru increased the ECSA exponentially, and it was three times higher than that of Pd/MWCNT. They found that the catalytic activity and

CO poisoning were 2.6 and 1.7 times greater than Pd/GNs in the basic medium under similar experimental conditions.[23]

According to the above discussion, graphene and its derivative-based catalysts have shown promising catalytic activity in fuel cells. However, the cost per gram of graphene is a concern, raising questions about its affordability as the catalytic support. Thus, several researchers are continuously preparing different types of carbon nanomaterials from plastic waste,[24] which not only suppresses the cost of graphene but also helps to solve other environmental problems. Various thermal technologies, such as pyrolysis,[25,26] gasification, chemical vapor deposition (CVD), and upcycling processes,[27] enable the conversion of waste plastics into CNMs and value-added products.[28,29] Among these, pyrolysis is the most appropriate and cost-effective method for reducing the volume of waste plastic and recovering more products such as CNMs (like graphene, graphene oxide (GO), and nitrogen-doped graphene (NGO)) for energy conversion devices and other applications.[30,31]

To date, limited research has been conducted on the synthesis and application of heteroatom-doped waste plastic-derived reduced graphene-based nanohybrids as electrocatalysts for oxygen reduction reaction (ORR) with a Pd–Ru composition. This work addresses pressing environmental issues, from waste mismanagement and the transition to green energy. It spotlights PEMFCs, highlighting challenges with expensive platinum catalysts. Innovatively, waste plastic-derived nitrogen-doped graphene oxide (WpNrGO) is introduced as a cost-effective catalyst support. WpNrGO-supported Pd–Ru in a 2:1 ratio with the core–shell decorated nanohybrid is an efficient metal catalyst for the PEMFCs, and the study combines affordability and performance. Density functional theory (DFT) validates the WpNrGO/Pd–Ru catalyst's efficacy, marking a crucial step toward sustainable, efficient energy solutions and waste-derived catalysts. The synthesized WpNrGO-Pd–Ru core–shell electrocatalyst showed increased catalytic activity, stability, and
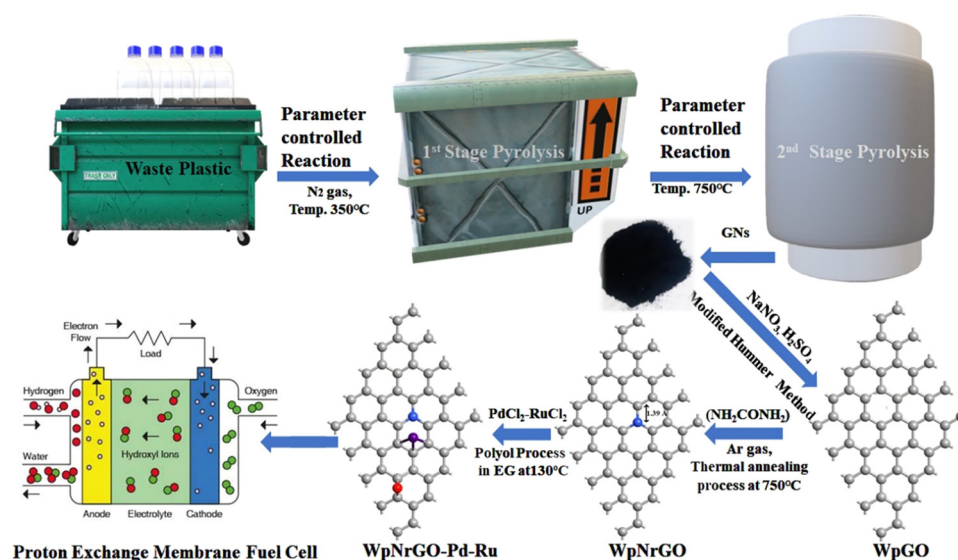

Fig. 1 Schematic of the complete process.

higher electrochemical surface (ECSA) area as compared to commercial catalysts (Pt/C) (Fig. 1).

2. Materials and method

2.1 Materials

Waste plastic-derived graphene nanosheet, potassium permanganate ($KMnO_4$), sodium nitrate ($NaNO_3$), urea (NH_2CONH_2), sulfuric acid (H_2SO_4), hydrochloric acid (HCl), sodium hydroxide (NaOH), hydrogen peroxide (H_2O_2 30% aq), palladium(II)chloride ($PdCl_2$), and ethylene glycol ($C_2H_6O_2$) were purchased from SRL, and silicone oil was purchased from Merck. Ruthenium chloride ($RuCl_2$) and commercially accessible Pt/C catalysts were obtained from Sigma Aldrich and used as received.

3. Experimental

3.1 Synthesis of graphene nanosheet and WpGO

Graphene nanosheet (GNs) is synthesized in the laboratory by upcycling waste plastic *via* pyrolysis, according to our previously reported method.[30,31] In addition, the GNs were subjected to further processing using the modified Hummers' method[32] to obtain waste plastic graphene oxide (WpGO). In this method, the GNs were treated with $NaNO_3$ and H_2SO_4 rather than the additional use of $KMnO_4$. To remove the impurities, 5% HCl was used to wash the obtained WpGO. Further, WpGO was washed with distilled water (DW) using centrifugation methods at 7000 rpm until the pH level reached neutral and dried in an oven at 80 °C.

3.2 Preparation of WpNrGO

WpNrGO was prepared by thermal annealing[33] at 750 °C in a tube furnace with urea (NH_2CONH_2) in an inert medium of Ar gas at a flow rate of 2.5 ccm s^{-1}. In this process, WpGO was treated with 20% (by weight of WpGO) NH_2CONH_2 at a temperature rate of 5% min^{-1}. The WpNrGO was collected after cooling down the reaction temperature and washed with 5%Cl and DW. After this, WpNrGO was kept for drying in the oven at 80 °C overnight.

3.3 Preparation of WpNrGO-Pd–Ru (2:1) metal catalyst

A polyol technique was used to prepare the WpNrGO-supported Pd–Ru electrocatalyst in an ethylene glycol (EG) solution.[9,34] Briefly, 80 mg of WpNrGO was dispersed in an EG solution and sonicated for an hour at ambient temperature. $PdCl_2$ (66.66 mg Pd) and $RuCl_3$ (133.33 mg Ru) were dispersed in 20 mL of ethylene glycol and sonicated for an hour to achieve a homogenous dispersion. Further, both solutions were mixed and then sonicated for 1 hour. Then, 15 mL of 1 M NaOH solution was added drop by drop in the above mixture to adjust the pH to 12. In order to attain a uniform dispersion of the metal nanoparticles inside the WpNrGO suspension, the mixture was stirred for 1 hour at 130 °C. The mixture was allowed to cool at room temperature and was maintained at pH 4 with the addition of ~20 mL of HCl. Later, it was centrifuged and

cleaned with DW to obtain the final WpNrGO-Pd–Ru nanohybrids (2:1). Further, the synthesized WpNrGO-Pd–Ru was dried in the oven at 80 °C overnight.

4. Characterizations

The synthesized WpGO, WpNrGO, and WpNrGO-Pd–Ru were investigated using various spectroscopic and microscopic techniques. The defects and quality of WpGO, WpNrGO, and WpNrGO-Pd–Ru nanohybrid were confirmed by Raman spectroscopy (Horiba Scientific xplora plus-532 nm). The Fourier transformation infrared spectroscopy (FT-IR) study was conducted to detect functional groups using the KBr pellet system (Model IR PerkinElmer, Spectrum 2000) within the scan ranges 400 and 4000 cm^{-1}. The degree of graphitization and crystallization in the WpGO, WpNrGO and WpNrGO-Pd–Ru nanohybrids was evaluated by X-ray diffraction (XRD) examination using a Rigaku Japan (Ultima IV X-ray diffractometer). The internal and external morphologies of synthesized nanohybrid were studied using transmission electron microscopy (TEM) (JEOL, JEM 2100) and scanning electron microscopy (SEM) (JOEL, Model-JSM-7610F), respectively.

4.1 Electrochemical measurements

The electrochemical measurements were carried out with AUTO LAB PGSTAT302N electrochemical system, using a conventional 3-electrode cell in 0.1 M H_2SO_4 electrolyte. Platinum wires and double-junction Ag/AgCl were employed as counter and reference electrodes, respectively. For the working electrode, 10 μL of synthesized nanohybrid dispersion in ethyl alcohol was drop-cast over the glassy carbon disk electrode. Prior to nanohybrid deposition, the glassy carbon electrode is polished with a 0.05 mm alumina suspension, then cleaned thoroughly with distilled water and dried in air for 30 minutes. The ECSA of the WpNrGO-Pd–Ru nanohybrid is calculated from the charge density of Pd and Ru q_{Pd-Ru} (C cm^{-2} electrode) obtained from the CV at very low catalyst loading (00.0976 mg cm^{-2}), where the conversion factors for Pt, Pd, and Ru are 210 C cm^{-2}, 424 C cm^{-2}, and 420 C cm^{-2}, respectively.

5. Result and discussion

Raman spectroscopy was conducted to examine the existence of defects in the number of layers and quality of WpGO, WpNrGO, and WpNrGO-Pd–Ru. The Raman spectra of these materials exhibit D and G bands, which are common in all (Fig. 2). However, WpNrGO and WpNrGO-Pd–Ru show the two overtone bands (2D and D′) along with D and G and are affected by the sensitivity of the restricted atomic arrangement.

The D band originates in WpGO, WpNrGO and WpNrGO-Pd–Ru due to their sp^3 carbon domain, which also indicates the defects in the graphene and its based materials. The G band arises due to the stretching of the C=C bond in such materials, which is very common to all conjugated carbon systems. The WpGO shows typical Raman spectra of GO with two significant
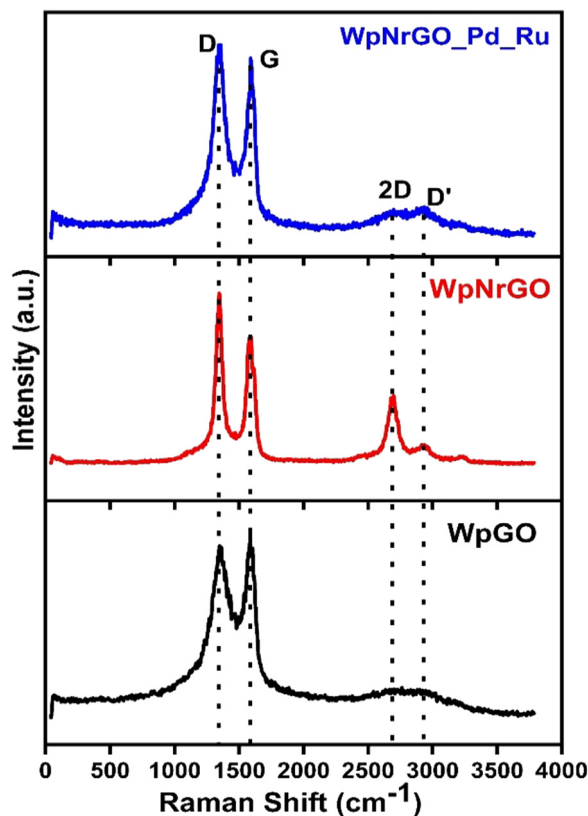
Fig. 2   Raman spectroscopy of WpGO, WpNrGO and WpNrGO-Pd–Ru.

peaks at 1353 cm^{-1} (D-band) and 1582 cm^{-1} (G-band), respectively. In the case of WpNrGO, the G band is less broadened and

shows a little blue shift, which is due to the appearance of a new 2D peak at 2767 cm^{-1}. Also, the intensity of the D band in WpNrGO is higher as compared to WpGO, which indicates the occurrence of more defects in WpNrGO.[35] The higher intensity of the D band also confirms the breakage of sp^2 and the formation of a new sp^3 carbon domain. Consequently, the higher intensity ratio of the D and G bands (I_D/I_G) shows that new defects arise in WpNrGO during the thermal annealing process. However, the Raman spectra of WpNrGO-Pd–Ru do not differ significantly from WpNrGO, except for a slight decrease and broadening in the intensity of the 2D and D′ peaks. This is attributed to the reduction in functional groups on WpNrGO, which occurred during the polyol process, as well as the introduction of Pd and Ru.[36]

In order to determine the presence of functional groups on WpGO, WpNrGO and WpNrGO-Pd–Ru, FT-IR was used, as shown in (Fig. 3a). FT-IR spectra showed peaks at 3402–3341 cm^{-1}, 2958–8261 cm^{-1}, 1720 cm^{-1}, 1530–1436 cm^{-1}, 1156 cm^{-1}, 1266 cm^{-1}, 1020 cm^{-1}, and 1600 cm^{-1} corresponding to O–H stretching vibrations, C–H stretching vibration, C=O (carbonyl/carboxy), C–N stretch, C–O group, C–O (alkoxy) and skeletal vibrations of un-oxidized graphite, respectively. The FTIR spectra of WpGO clearly show the O–H stretching vibration peak at 3402–3341 cm^{-1}, which disappears in WpNrGO and WpNrGO-Pd–Ru due to the high-temperature annealing and Pd–Ru incorporation processes. Also, due to these synthesis processes, epoxy and hydroxyl groups were significantly decreased in WpNrGO and WpNrGO-Pd–Ru; however, the major peak of C–N stretch is found in the range between 1467 cm^{-1} and 1436 cm^{-1}.[37–39]

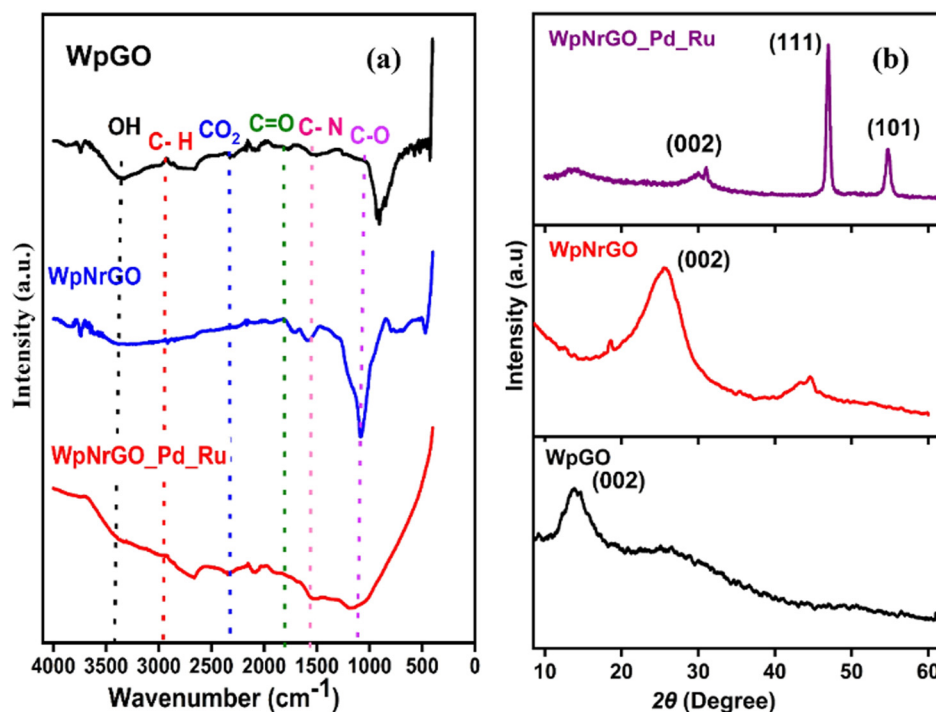Fig. 3b shows the XRD pattern of WpGO, WpNrGO, and WpNrGO-Pd–Ru. The WpGO shows a broad and sharp peak at

Fig. 3   (a) FT-IR spectra of WpGO, WpNrGO, and WpNrGO-Pd–Ru. (b) XRD pattern of WpGO, WpNrGO, and WpNrGO-Pd–Ru.

© 2024 The Author(s). Published by the Royal Society of Chemistry

12°, which corresponds to the (111) plane with an interlayer d-spacing of 6.822 Å. Such an enlarged interlayer distance between the layers is due to the intercalation of oxygen functional groups, which indicates the chemical oxidation of WpGO. However, the XRD diffraction peak at 27.6° in WpNrGO is due to the presence of defects on the surface of WpGO, whereas a peak at 30° concerning the (220) interlayer spacing is attributed to the intercalation of nitrogen atoms over its surface (Fig. 3b). Similarly, WpNrGO-Pd–Ru shows a broad diffraction peak in the range of 12° to 85°, along with the broad feature in the low-angle scattering region, suggesting that nanocrystallites with an XRD pattern of nanoparticles of palladium (JCPDS card No. 75-584) and ruthenium (JCPDS card No. 6-663).[40,41] The average crystallite size of the metallic palladium nanoparticle with an average size of 2 nm with (200) interlayer d spacing of 2.09 Å and ruthenium nanoparticle with an average particle size of 2–3 nm concerning the plane of (102) and (103) interlayer distance of 1.6 Å (Fig. 3b).

(Fig. 4a, d and g) depict SEM images of WpGO, WpNrGO, and WpNrGO-Pd–Ru. (Fig. 4a) showed the SEM image of WpGO that indicated the combination of thin and thick crumpled layers or sheet-type structures, which were generated due to the oxidation of GNs into WpGO.[42,43]

Similarly, WpNrGO has an irregularly wrinkled silk veil wave orientation with stacks of sheets. These sheets have rippled and become entangled with each other. This could have occurred due to the removal of oxidative groups during the nitrogen doping process at high temperatures and an increase in the van der Waals interactions between the sheets of WpNrGO. These sheets appear translucent with lateral diameters ranging from 2–6 nm to several μm.[44] Further, (Fig. 4g and 5a and b) show the SEM images of WpNrGO-Pd–Ru. These images show the distribution of Pd and Ru all over the surface of WpNrGO. (Fig. 4b, e and h) depict the surface topology for WpGO, WpNrGO, and WpNrGO-Pd–Ru. (Fig. 4b) demonstrates a sheet-shaped structure for WpGO, while the WpNrGO (Fig. 4e) shows a few upraised needled shapes in the WpGO sheets due to doping and intercalation of nitrogen atoms, which perturb the sheet structure. (Fig. 4h) depicts the final core–shell structure of the composite material with submerged Pd and Ru in the WpNrGO sheet and exhibits an excellent distribution. The continual changes are visible in the sheet structure of WpNrGO, with several dotted structures showing the immersion of both metals. Further, the evaluations were elaborated on with corresponding hill stack plots for each material, viz WpGO, WpNrGO, and WpNrGO-Pd–Ru. Hill stack plots displayed a clear structure of the surface in a 3D display showing the topologic view from the top position for each structure, where WpGO is displayed as a dense arrangement of layers, while WpNrGO is displayed as separated stacked layers of WpGO, and broadly condensed structure showing the immersion of both metals to develop a core–shell structure of the composite in WpNrGO-Pd–Ru (Fig. 4c, f and i).

Moreover, TEM was studied to find out the structural surface morphology of synthesized WpGO, WpNrGO, and WpNrGO-Pd–Ru. (Fig. 6), shows a comprehensible structural analysis of WpGO, WpNrGO, and WpNrGO-Pd–Ru, depicting their internal
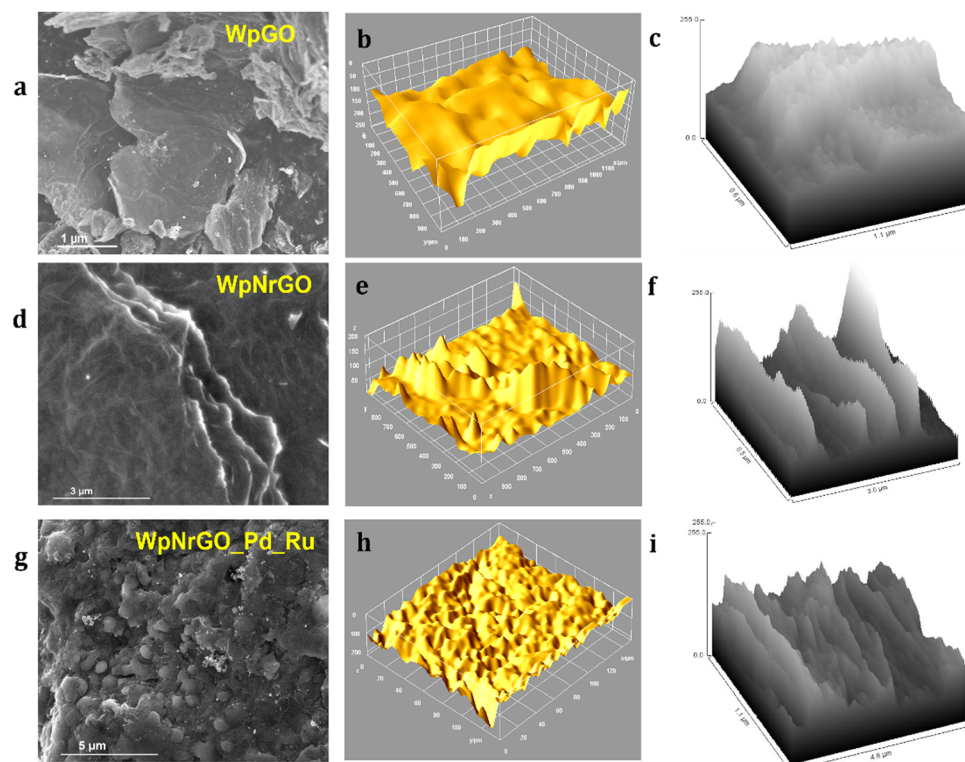
Fig. 4 SEM images of (a) WpGO, (d), WpNrGO, and (g) WpNrGO-Pd–Ru; 3D surface topology from the SEM analysis of (b) WpGO, (e) WpNrGO, and (h) WpNrGO-Pd–Ru; hill stack plot of (c) WpGO, (f) WpNrGO, and (i) WpNrGO-Pd–Ru.
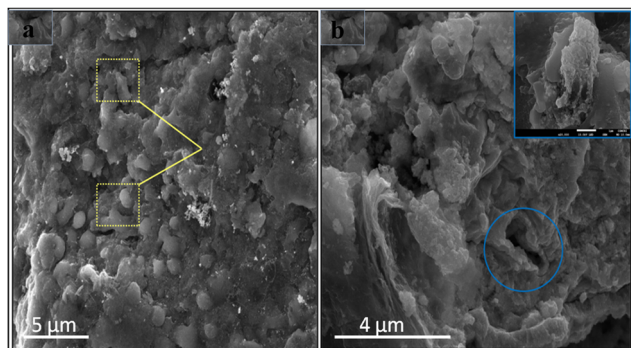
Fig. 5 SEM images: (a) distribution of Pd/Ru over the WpNrGO sheet. (b) Core–shell structure and domain arrangement of nanoparticles on WpNrGO-Pd–Ru.

thick flat flake layers, rough surfaces, and irregular shapes with non-uniform particle sizes. The disorder and unwrinkled shape suggested the presence of oxygenated functional groups during the exfoliation and oxidation process.[45,46] The TEM image in (Fig. 7a) exhibits multilayer patterns that might be attributed to the defective structures during exfoliation, as well as the presence of external nitrogen atoms. Furthermore, the TEM pictures of the foldable graphene layers on one edge reveal isolated small fragments on the surfaces.[47,48]

The high-resolution HRTEM image has revealed the conformation of the deposit and distribution of Pd and Ru nanoparticles on the WpNrGO sheet (Fig. 7a–d). TEM image of WpNrGO depicted in (Fig. 7a) showed a sheet-like structure while (Fig. 7b and c) shows the distribution of Pd–Ru in WpNrGO-Pd–Ru sheets as dotted spots, further confirmed in elemental analysis of the composite material depicting the presence of Pd, and Ru with carbon, nitrogen, and oxygen (Fig. 7d). In contrast, Pd and Ru particles of are aggregated and located meagerly on the graphene surface with a broad particle size distribution. However, the d spacing value of TEM analysis shows good agreement with the d value of XRD $2d \sin \theta = n\lambda$ data. In this sequence, the distribution of Pd and Ru in WpNrGO-Pd–Ru has been further confirmed by EDS analysis in (Fig. 7d), where the distribution of Pd and Ru is 14.54 wt% and 8.88 wt%, respectively. Further DFT was

structure and hill stack pattern. A clear distinction in internal structure visible in TEM images, *viz.* relatively separate layers for WpGO, more closed layers for WpNrGO, and dense composite arrangements with possibly submerged Pd and Ru are visible in internal analysis and hill stack pattern of WpNrGO-Pd–Ru (Fig. 6a–i).

TEM images revealed that more than one layer of material was present in the synthesized powder sample. WpGO (Fig. 7a) appears almost transparent and the morphology comprises
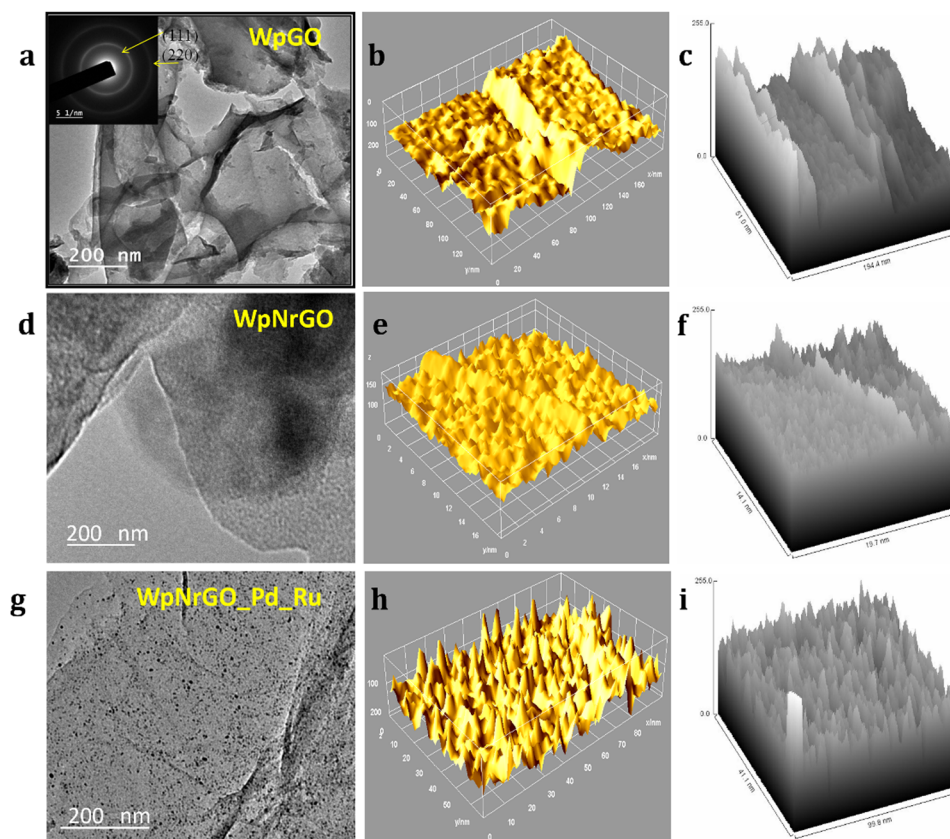

Fig. 6 TEM images of (a) WpGO, (d) WpNrGO, and (g) WpNrGO-Pd–Ru; internal 3D structure from the TEM analysis of (b) WpGO, (e) WpNrGO, and (h) WpNrGO-Pd–Ru; Hill stack plot of (c) WpGO, (f) WpNrGO, and (i) WpNrGO-Pd–Ru.
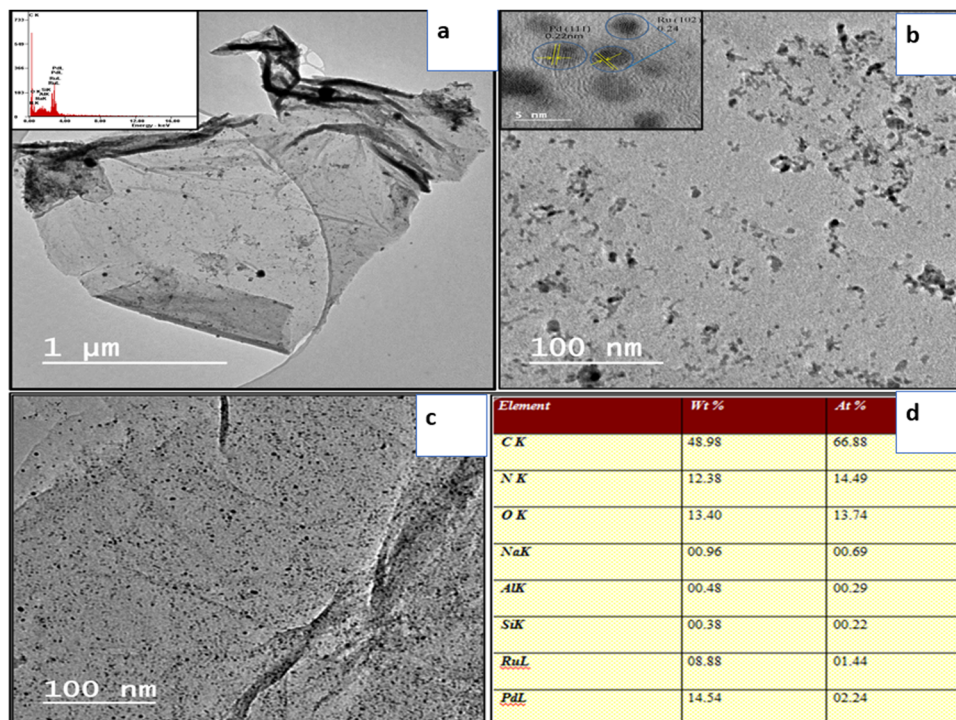
Element	Wt %	At %
C K	48.98	66.88
N K	12.38	14.49
O K	13.40	13.74
NaK	00.96	00.69
AlK	00.48	00.29
SiK	00.38	00.22
RuL	08.88	01.44
PdL	14.54	02.24

Fig. 7 (a) HRTEM image of WpNrGO, (b) and (c) distribution of Pd–Ru in WpNrGO-Pd–Ru, and (d) the concentration of Pd and Ru.

performed to evaluate and confirm the doping possibilities of N, Pd, and Ru on the surface of WpGO.

5.1 Density functional theory (DFT) analysis

The EDS analysis showed the presence of N, Pd, and Ru as the dopants in WpNrGO-Pd–Ru. Thus, using Synopsys-QuantumATK, first-principles simulations based on density functional theory (DFT) were performed to identify the optimal locations for these dopants to adsorb on WpNrGO (N) and WpNrGO-Pd–Ru (N, Pd and Ru).[49] The Local Density Approximation (LDA) tool is used to define the exchange–correlation interaction energy of electrons. The valence electrons are described using the localized Double Zeta Polarized (DZP) basis sets, with a density mesh cutoff of 75 Hartree. A $6 \times 6 \times 1$ Monkhorst–Pack grid of K-points is used to conduct the structural relaxations of the 5×5 supercells. A sufficient vacuum padding of 10 Å has been considered in the non-periodic directions to avoid interactions among the mirror images. The structural relaxations (optimizations) are carried out using the Limited memory Broyden–Fletcher–Goldfarb–Shanno (L-BFGS) algorithm[50,51] to obtain stress and force tolerance levels of 0.05 eV Å^{-3} and 0.05 eV Å^{-1}, separately. Initially, various possible adsorption cases of nitrogen on WpGO in WpNrGO have been analyzed for their thermodynamic stability. In case-1, nitrogen is adsorbed on the bond site (C=C bond) of WpGO. In case 2, nitrogen is adsorbed on the hollow site of the carbon ring of WpGO. In case 3, nitrogen is adsorbed on top of the carbon atom of the WpGO. In case-4, nitrogen is adsorbed at a single vacancy defect site of WpGO in the graphitic pattern. In case-5, nitrogen is adsorbed at the double vacancy defect site of WpGO in a pyridinic pattern. In case 6, nitrogen is adsorbed at the

hexa-vacancy defect site of WpGO in the pyrrolic pattern. The structure of the WpNrGO sheet for each adsorption case before and after optimization is shown in (Fig. 8). The corresponding formation energy per unit length of the sheet (E_F^L) is also given in (Fig. 8) for each adsorption case, which offers information about the relative thermodynamic stability of the structure. A low formation energy indicates the relatively high thermodynamic stability of the structure in comparison to its counterparts. The formation energy per unit length is calculated using the expression given below.

$$E_F^L = \frac{\left[E_{\text{N adsorbed sheet}} - xE_C - y\frac{E_{N_2}}{2} \right]}{L} \qquad (1)$$

Here, $E_{\text{N adsorbed sheet}}$, E_C and E_{N_2} refer to the energies of the nitrogen-adsorbed WpGO in WpNrGO, the carbon atom of WpGO, and nitrogen gas, respectively. x indicates the number of carbon atoms, and y indicates the number of nitrogen atoms in the sheet. L is the sheet length, which is approximately $\sim$12.30 Å.

As seen from (Fig. 8), the formation energies for various nitrogen adsorption cases *viz.* bridge site (case-1), hollow site of carbon ring (case-2), top of carbon atom (case-3), at single vacancy site in graphitic pattern (case-4), at double vacancy site in pyridinic pattern (case-5), and hexa-vacancy site in pyrrolic pattern (case-6) are 0.31 eV Å^{-1}, unstable adsorption, 0.31 eV Å^{-1}, -0.02 eV Å^{-1}, 0.39 eV Å^{-1}, and 1.27 eV Å^{-1}, respectively. The N adsorption at the hollow site (case-2) is treated unstable as this site offers no affinity towards the adsorbed nitrogen. The unstable
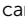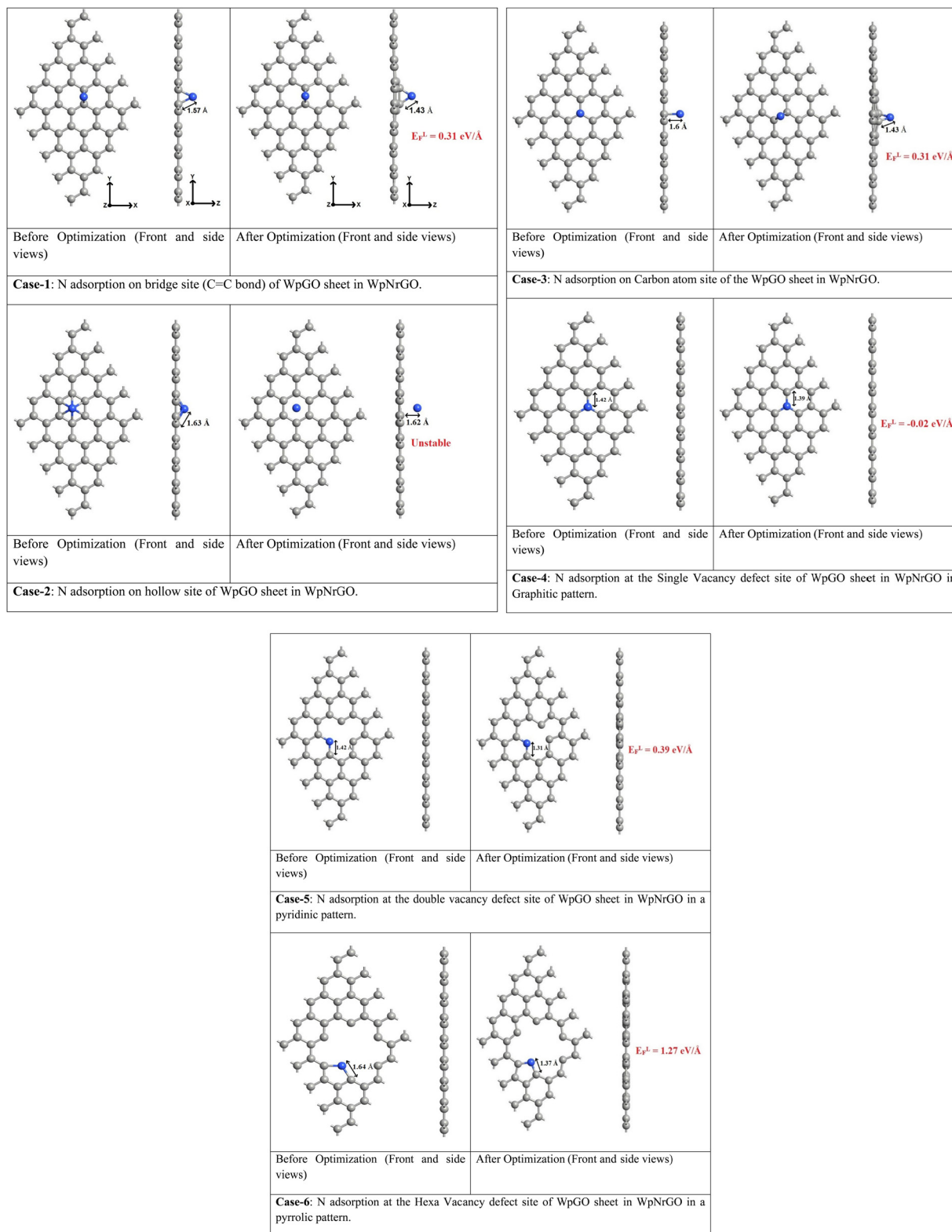
Before Optimization (Front and side views) | After Optimization (Front and side views)

Case-1: N adsorption on bridge site (C=C bond) of WpGO sheet in WpNrGO.

$E_F^L = 0.31$ eV/Å (Case-1, after optimization, 1.43 Å; before 1.57 Å)

Case-3: N adsorption on Carbon atom site of the WpGO sheet in WpNrGO.

$E_F^L = 0.31$ eV/Å (Case-3, before 1.6 Å; after 1.43 Å)

Case-2: N adsorption on hollow site of WpGO sheet in WpNrGO.

(Case-2, before 1.63 Å; after 1.62 Å — Unstable)

Case-4: N adsorption at the Single Vacancy defect site of WpGO sheet in WpNrGO in Graphitic pattern.

$E_F^L = -0.02$ eV/Å (Case-4, before 1.42 Å; after 1.39 Å)

Case-5: N adsorption at the double vacancy defect site of WpGO sheet in WpNrGO in a pyridinic pattern.

$E_F^L = 0.39$ eV/Å (Case-5, before 1.42 Å; after 1.31 Å)

Case-6: N adsorption at the Hexa Vacancy defect site of WpGO sheet in WpNrGO in a pyrrolic pattern.

$E_F^L = 1.27$ eV/Å (Case-6, before 1.64 Å; after 1.37 Å)

Fig. 8 Various possible adsorption cases of N on a graphene sheet. Color code: ● carbon, ● nitrogen.

case-3 turned into the stable case-1 after optimization. This implies that only the bridge site (C=C bond site) offers good affinity for nitrogen in the defect-free WpGO sheet. However, all the defective WpGO offer good affinity towards nitrogen, as witnessed from case 4 to case 6. In case-4, case-5, and case-6, the side views of the optimized structures show a perfect planar

arrangement of carbon atoms, indicating that the carbons have retained their sp^2 hybridization even after the creation of defect and adsorption of nitrogen. However, in case-1 and case-3, the side view of optimized structures reveals that the two carbon atoms supporting the nitrogen are slightly plucked out of the plane, indicating a possible hybridization change in these two atoms from sp^2 to sp^3. Out of all the possible nitrogen adsorption cases, the graphitic pattern (case-4) exhibits the relatively lowest formation energy of -0.02 eV Å^{-1}, and thereby the highest stability. This implies that the majority of the nitrogen atoms present in the WpGO might have undergone a graphitic pattern of doping during the synthesis of WpNrGO. Prompted by these results, we have used the graphitic patterned WpNrGO to understand the positioning of palladium (Pd) and ruthenium (Ru) dopants below.

(Fig. 9a and b) show the adsorption of Pd and Ru dopants on the WpNrGO sheet in WpNrGO-Pd–Ru, respectively. Here, the

Pd/Ru dopant is placed just above the graphitic nitrogen of WpNrGO before the optimization to assess the influence of the nitrogen dopant on Pd/Ru dopants. The formation energy for Pd/Ru adsorption is calculated using eqn (2) given below.

$$E_{\mathrm{F}}^{L} = \frac{[E_{\mathrm{Pd\ or\ Ru\ adsorbed\ NGO}} - E_{\mathrm{NGO}} - E_{\mathrm{Pd\ or\ Ru}}]}{L} \qquad (2)$$

From (Fig. 9), the calculated formation energies are very low, indicating a very stable reaction between Pd/Ru and the WpNrGO sheet. It is worth noting that the Pd/Ru dopants bond only with the carbon atoms of WpNrGO after optimization, even though they were placed over the graphitic nitrogen atom before the optimization. It indicates that the graphitic nitrogen with an intrinsic lone pair is pretty stable and unwilling to entertain the Pd/Ru dopant. Thus, the Pd/Ru dopants are accommodated by the carbon skeleton of WpNrGO and the
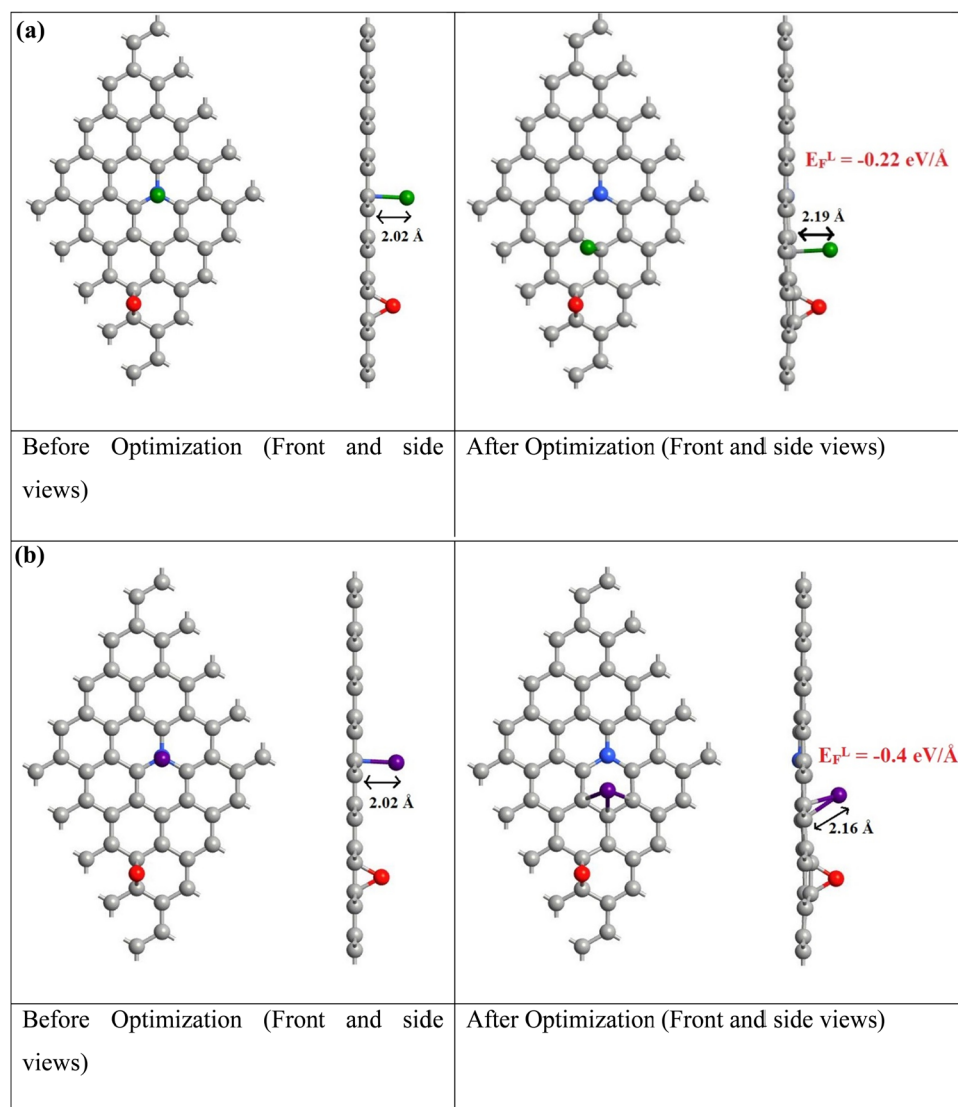

Fig. 9 (a) Pd adsorption on the graphitic patterned WpNrGO sheet. (b) Ru adsorption on the graphitic patterned WpNrGO sheet in WpNrGO-Pd–Ru. Color code: ● carbon, ● nitrogen, ● oxygen, ● palladium, ● ruthenium.

presence of nitrogen does not enhance the accommodation of these dopants. This may be one of the reasons behind the low atomic percentage of Pd (2.24%) and Ru (1.44%) dopants in the synthesized WpNrGO-Pd–Ru composite, given the fact that the nitrogen is present in a large quantity (14.49%) in WpNrGO. However, the presence of graphitic nitrogen in WpNrGO enhances its electronic properties owing to the rich chemistry of nitrogen with carbon and the inherent lone pair. To summarize the discussion of computational results, the graphitic form of nitrogen doping may be prominent in the synthesized WpNrGO. Moreover, the Pd/Ru dopants are bound to the carbon skeleton of WpNrGO, as the nitrogen atoms do not offer any affinity to them.

5.2 Electrochemical analysis

The electrochemical study was carried out through the three-electrode system. The WpNrGO-Pd–Ru or commercial Pt/C (for comparison study), Pt wire and Ag/AgCl were used as a working, counter and reference electrode, respectively. The cyclic voltammetry was performed at the scan rate of 10 mV s^{-1} to 500 mV s^{-1} between −0.2 V and 1.0 V in 0.1 M H$_2$SO$_4$ aqueous electrolyte. Initially, the commercial Pt/C as a working electrode was tested and further compared with WpNrGO-Pd–Ru at similar electrochemical parameters *viz.* scan rate of 500 mV s^{-1} with a potential window between −0.2 V and 1.0 V (Fig. 10a and b). The comparative plot displayed a higher current response and very high ECSA of WpNrGO-Pd–Ru as compared to the commercial Pt/C. ECSA results are strongly evident in the determination

of the performance of the WpNrGO-Pd–Ru (2 : 1 ratio) core–shell nanohybrid as a catalyst for anode and cathode. The ECSA was nonetheless obtained by integrating the area under the curve in the vicinity of hydrogen adsorption and desorption after double-layer correction. According to the CV analysis for the ECSA assessment, the WpNrGO-Pd–Ru 2 : 1 core–shell electrocatalyst demonstrated a better mass-specific ECSA value of ∼43 m^2 g^{-1} than the commercial Pt/C value of ∼36 m^2 g^{-1} at extremely low catalyst loading (00.0976 mg cm^{-2}). To do this, the ECSA of the WpNrGO-Pd–Ru catalyst is calculated from the charge density of Pd and Ru $q_{Pd–Ru}$ (C cm^{-2} electrode) obtained from the CV, where the conversion factors for Pt, Pd, and Ru are 210 C cm^{-2}, 424 C cm^{-2} and 420 C cm^{-2} respectively. The metal loading in the electrode L in g Pd–Ru per cm^2.

$$ECSA = \frac{q_{Pd–Ru}}{\Gamma \cdot L} \qquad (3)$$

Furthermore, the experimental results proposed that exceptional ECSA was achieved by the doping of nitrogen in WpNrGO. The lone pair of electrons in nitrogen provides an electron transport system for Pd and Ru metal nanocatalyst. Therefore, the results endorsed high surface area and better stability. Stability assessments were made by evaluating electrodes after 6000 cycles, which displayed excellent retention of ECSA performance. (Fig. 10c) shows high stability for WpNrGO-Pd–Ru, which was tested up to 6000 cycles at 500 mV s^{-1} with a potential window of 1.2 V. The stable alignment of each CV cycle predicts
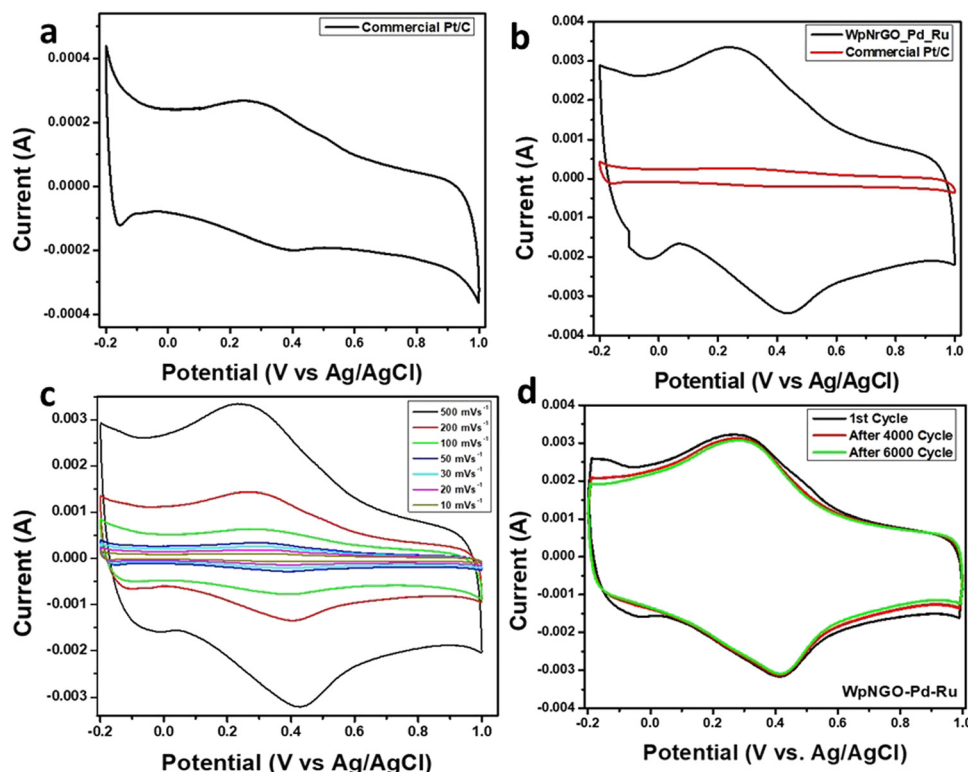

Fig. 10 (a) CV curves of commercial Pt/C (0.1 M H$_2$SO$_4$, scan rate 500 mV s^{-1}). (b) CV curves of WpNrGO-Pd–Ru and commercial Pt/C at 500 mV s^{-1} (Pd–Ru loading 0.0976 mg cm^{-2}). (b) CV curves of WpNrGO-Pd–Ru at different scan rates. (d) CV curves after 1, 4000, and 6000 cycles (0.1 M H$_2$SO$_4$).

Table 1 ECSA and stability of the synthesized WpNrGO-Pd–Ru catalyst compared with the catalysts reported literature

S. No.	Catalyst	ECSA ($m^2\ g^{-1}$)	Stability (cycles/hours)	Ref.
1	Pt–B–Gr/CB (30%)	33.6	1200	52
2	PtNW-Pd/rGO	19	200	53
3	Au/rGO	12.9	9200	54
4	Pd_3Co/N-G	39.8	—	55
5	PdRu/MWCNT-GNP	20.7	—	56
6	Pd/C	43	—	57
7	Pd/untreated-MWCNT	21.4	—	58
8	Pd/acid-oxidized MWCNT	35.7	—	58
9	Pt/GO	13.62	5000 (19%)	59
10	Pt/G	8.2		60
11	Pt/BG-1 (reduction by $NaBH_4$)	17.8		60
12	Pt/BG-2 (polyol method)	30.0		60
13	Pt/BG-3 (modified polyol method)	46.9	50 hours	60
14	Pt/rGO	0.51	1000 (49%)	61
15	Pt/GO-r	1.11	1000 (50%)	61
16	Pt/GO	0.62	1000 (50%)	61
17	Pt/C	$\sim 36\ m^2\ g^{-1}$	5000	Present study
18	WpNrGO-Pd–Ru	$\sim 43\ m^2\ g^{-1}$	5000	Present study

Note: Pt–B–Gr/CBx: Pt-boron doped graphene/carbon black; NW: nanowire; Pd_3Co/NG: palladium–cobalt supported nitrogen-doped rGO; PdRu/MWCNT-GNP: palladium–ruthenium (PdRu) supported on multiwalled carbon nanotube-graphene; Pt/G: platinum/graphene; Pt/BG: platinum/boron-doped graphene; Pt/GO-r: platinum/partially reduced graphene oxide (GO-r).

high stability that can be attributed to the electron mobility and charge carrier of nitrogen-doped graphene oxide support.

Further, results obtained in terms of ECSA and stability from the prepared catalysts were compared with the previously reported literature (Table 1). The comparison results indicate the utility and importance of the prepared catalyst for PEMFCs.

6. Conclusion

The waste plastic GNs are obtained from the pyrolysis of waste plastic, followed by the modified Hummers' method to obtain WpGO, which is further doped with nitrogen through the thermal annealing process. However, the WpNrGO-Pd–Ru prepared from the polyol process showed a core–shell structure, and the Pd and Ru nanoparticles are immersed in the WpNrGO sheet. Pd and Ru nanoparticles exhibit excellent homogeneous distribution. The WpNrGO-Pd–Ru shows incomparable electrochemical activity and electrochemical stability before and after 6000 cycles of ORR activity compared to commercial Pt/C. The observed result reveals that WpNrGO-Pd–Ru shows much higher ECSA $\sim 43\ m^2\ g^{-1}$ than commercial Pt/C $\sim 36\ m^2\ g^{-1}$.

Conflicts of interest

The authors state no opposing interests.

References

1 D. Das and T. N. Veziroglu, *Int. J. Hydrogen Energy*, 2008, **21**, 6046–6057.
2 E. Eroğlu, İ. Eroğlu, U. Gündüz, L. Türker and M. Yücel, *Int. J. Hydrogen Energy*, 2006, **31**, 1527–1535.
3 R. Nandi and S. Sengupta, *Crit. Rev. Microbiol.*, 1998, **24**, 61–84.
4 P. Loyselle and K. Prokopius, Teledyne Energy Systems, Inc., Proton Exchange Member (PEM) Fuel Cell Engineering Model Powerplant. Test Report: Initial Benchmark Tests in the Original Orientation 2011; (No. NASA/TM-2011-216225).
5 P. Fal, O. Troshina and P. Lindblad, *Int. J. Hydrogen Energy*, 2002, **27**, 1209–1215.
6 B. D. McNicol, D. A. J. Rand and K. R. Williams, *J. Power Sources*, 2001, **100**, 47–59.
7 E. Antolini, *Appl. Energy*, 2011, **88**, 4274–4293.
8 S. Park, J. M. Vohs and R. J. Gorte, *Nature*, 2000, **404**, 265–267.
9 S. Dhali, M. Karakoti, S. Pandey, B. SanthiBhushan, R. K. Verma, A. Srivastava, R. Bal, S. P. S. Mehta and N. G. Sahoo, *Int. J. Hydrogen Energy*, 2020, **45**, 18704–18715.
10 S. Dhali, S. Pandey, A. Dandapat, T. Sahoo, P. S. Sahu, B. Saha and N. G. Sahoo, *Diamond Relat. Mater.*, 2022, **126**, 109115.
11 P. Chen, T. Y. Xiao, Y. H. Qian, S. S. Li and S. H. Yu, *Adv. Mater.*, 2013, **25**, 3192–3196.
12 Y. Wang, Y. Shao, D. W. Matson, J. Li and Y. Lin, *ACS Nano*, 2010, **4**, 1790–1798.
13 A. L. M. Reddy, A. Srivastava, S. R. Gowda, H. Gullapalli, M. Dubey and P. M. Ajayan, *ACS Nano*, 2010, **4**, 6337–6342.
14 L. S. Zhang, X. Q. Liang, W. G. Song and Z. Y. Wu, *Phys. Chem. Chem. Phys.*, 2010, **12**, 12055–12059.
15 C. S. Ramirez-Barria, M. Isaacs, C. Parlett, K. Wilson, A. Guerrero-Ruiz and I. Rodríguez-Ramos, *Catal. Today*, 2020, **357**, 8–14.

16 C. Zhang, J. Sha, H. Fei, M. Liu, S. Yazdi, J. Zhang, Q. Zhong, X. Zou, N. Zhao, H. Yu and Z. Jiang, *ACS Nano*, 2017, **11**, 6930–6941.

17 H. W. Liang, W. Wei, Z. S. Wu, X. Feng and K. Müllen, *J. Am. Chem. Soc.*, 2013, **35**, 16002–16005.

18 Y. C. Liu, Y. H. Hung, S. F. Liu, C. H. Guo, T. Y. Liu, C. L. Sun and H. Y. Chen, *Sustainable Energy Fuels*, 2020, **4**, 5339–5351.

19 H. Fang, T. Huang, Y. Sun, B. Kang, D. Liang, S. Yao, J. Yu, M. M. Dinesh, S. Wu, J. Y. Lee and S. Mao, *J. Catal.*, 2019, **371**, 185–195.

20 L. Dong, R. R. S. Gari, Z. Li, M. M. Craig and S. Hou, *Carbon*, 2010, **48**, 781–787.

21 R. Awasthi and R. N. Singh, *Carbon*, 2013, **51**, 282–289.

22 C. Zhuo and Y. A. Levendis, *J. Appl. Polym. Sci.*, 2014, **131**, 39931.

23 W. A. Qazi, M. F. Abushammala and M. H. Azam, *Waste Manage. Res.*, 2018, **36**, 594–605.

24 B. C. Liu, T. J. Lee, S. H. Lee, C. Y. Park and C. J. Lee, *Chem. Phys. Lett.*, 2003, **377**, 55–59.

25 P. K. Tripathi, S. Durbach and N. J. Coville, *Nanomaterials*, 2017, **7**, 284.

26 N. Patni, P. Shah, S. Agarwal and P. Singhal, *Int. Sch. Res. Notices*, 2013, **2013**, 7.

27 G. Tatrari, C. Tewari, B. S. Bohra, S. Pandey, M. Karakoti, S. Kumar, H. Tiwari, S. Dhali and N. G. Sahoo, *Clean. Eng. Technol.*, 2021, **5**, 100275.

28 N. Cai, S. Xia, X. Zhang, Z. Meng, P. Bartocci, F. Fantozzi, Y. Chen, H. Chen, P. T. Williams and H. Yang, *Chem-SusChem*, 2020, **13**, 938–944.

29 D. Guo, R. Shibuya, C. Akiba, S. Saji, T. Kondo and J. Nakamura, *Science*, 2016, **35**, 361–365.

30 S. Pandey, M. Karakoti, S. Dhali, N. Karki, B. SanthiBhushan, C. Tewari, S. Rana, A. Srivastava, A. B. Melkani and N. G. Sahoo, *Waste Manage.*, 2019, **88**, 48–55.

31 M. Karakoti, S. Pandey, G. Tatrari, P. S. Dhapola, R. Jangra, S. Dhali, M. Pathak, S. Mahendia and N. G. Sahoo, *Mater. Adv.*, 2022, **3**(4), 2146–2157.

32 W. S. Hummers Jr and R. E. Offeman, *J. Am. Chem. Soc.*, 1958, **80**, 1339.

33 Z. Mou, X. Chen, Y. Du, X. Wang, P. Yang and S. Wang, *Appl. Surf. Sci.*, 2011, **258**(5), 1704–1710.

34 S. A. Elsherif, E. N. El Sawy and N. A. A. Ghany, *J. Electroanal. Chem.*, 2020, **856**, 113601.

35 A. Eckmann, A. Felten, A. Mishchenko, L. Britnell, R. Krupke, K. S. Novoselov and C. Casiraghi, *Nano Lett.*, 2012, **12**, 3925–3930.

36 K. K. H. De Silva, P. Viswanath, V. K. Rao, S. Suzuki and M. Yoshimura, *J. Phys. Chem. C*, 2021, **25**, 7791–7798.

37 P. Sepideh, V. Mohammad Reza and R. Alimorad, *Surf. Coat. Technol.*, 2017, **311**, 282–294.

38 S. Sudhakar, K. K. Jaiswal, S. G. Peera and A. P. Ramaswamy, *Int. J. Recent Sci. Res.*, 2017, **8**, 19049–19053.

39 J. W. Hu, J. F. Li, B. Ren, D. Y. Wu, S. G. Sun and Z. Q. Tian, *J. Phys. Chem. C*, 2007, **111**, 1105–1112.

40 R. G. González-Huerta, R. González-Cruz, S. Citalán-Cigarroa, C. Montero-Ocampo, J. Chavez-Carvayar and O. Solorza-Feria, *J. New Mater. Electrochem. Syst.*, 2005, **8**, 15–23.

41 K. Kim, Z. Lee, B. D. Malone, K. T. Chan, B. Alemán, W. Regan, W. Gannett, M. F. Crommie, M. L. Cohen and A. Zettl, *Phys. Rev. B: Condens. Matter Mater. Phys.*, 2011, **83**, 245433.

42 Y. Feng, C. He, Y. Wen, Y. Ye, X. Zhou, X. Xie and Y. W. Mai, *J. Hazard. Mater.*, 2018, **346**, 140–151.

43 G. Tatrari, M. Karakoti, C. Tewari, S. Pandey, B. S. Bohra, A. Dandapat and N. G. Sahoo, *Mater. Adv.*, 2021, **2**, 1454–1484.

44 D. Geng, S. Yang, Y. Zhang, J. Yang, J. Liu, R. Li, T. K. Sham, X. Sun, S. Ye and S. Knights, *Appl. Surf. Sci.*, 2011, **257**, 9193–9198.

45 Y. Ma, L. Sun, W. Huang, L. Zhang, J. Zhao, Q. Fan and W. Huang, *J. Phys. Chem. C*, 2011, **115**, 24592–24597.

46 C. Androulidakis, E. N. Koukaras, J. Rahova, K. Sampathkumar, J. Parthenios, K. Papagelis, O. Frank and C. Galiotis, *ACS Appl. Mater. Interfaces*, 2017, **9**, 26593–26601.

47 Y. Sui, B. Zhu, H. Zhang, H. Shu, Z. Chen, Y. Zhang, Y. Zhang, B. Wang, C. Tang, X. Xie and G. Yu, *Carbon*, 2015, **81**, 814–820.

48 K. Gong, F. Du, Z. Xia, M. Durstock and L. Dai, *Science*, 2009, **323**, 760–764.

49 Quantum ATK, Synopsys Quantum Wise A/S, **https://www.synopsys.com/silicon/quantumatk.html**; 2021 [accessed 4 July 2021].

50 D. C. Liu and J. Nocedal, *Math. Program*, 1989, **45**, 503–528.

51 A. Srivastava and B. SanthiBhushan, *Appl. Nanosci.*, 2018, **8**, 637–644.

52 H. N. Yang, D. C. Lee, K. W. Park and W. J. Kim, *Energy*, 2015, **89**, 500–510.

53 P. Mardle, O. Fernihough and S. Du, *Coatings*, 2018, **8**, 48.

54 A. Marinoiu, M. Andrulevicius, A. Tamuleviciene, T. Tamulevicius, M. Raceanu and M. Varlam, *Appl. Surf. Sci.*, 2020, **504**, 144511.

55 P. Chandran, A. Ghosh and S. Ramaprabhu, *Sci. Rep.*, 2018, **8**, 3591.

56 T. M. H. Msrhad, Y. Devrim, A. Uzundurukan and Y. Budak, *Int. J. Energy Res.*, 2022, **46**, 4156–4173.

57 D. D. Tu, B. Wu, B. X. Wang, C. Deng and Y. Gao, *Appl. Catal., B*, 2011, **103**, 163–168.

58 C. G. Hu, Z. Y. Bai, L. Yang, J. Lv, K. Wang, Y. M. Guo, Y. X. Cao and J. G. Zhou, *Electro. Chim. Acta*, 2010, **55**, 6036–6041.

59 M. Lei, Z. B. Wang, J. S. Li, H. L. Tang, W. J. Liu and Y. G. Wang, *Sci. Rep.*, 2014, **4**, 7415.

60 A. Pullamsetty, M. Subbiah and R. Sundara, *Int. J. Hydrogen Energy*, 2015, **40**, 10251–10261.

61 J. Kim, S. I. Kim, S. G. Jo, N. E. Hong, B. Ye, S. Lee, H. S. Dow, D. H. Lee and J. W. Lee, *Catal. Today*, 2020, **352**, 10–17.